Opto-Electronic Science

Supplementary information

xxxx 2025, Vol. x, No. x

DOI: 10.29026/oes.2025.240034 CSTR: 32246.14.oes.2025.240034

Broadband ultrasound generator over fiber-optic tip for in vivo emotional stress modulation

Jiapu Li[2†], Xinghua Liu[1,3†*], Zhuohua Xiao[2†], Shengjiang Yang[2], Zhanfei Li[1,3], Xin Gui[4], Meng Shen[5], He Jiang[2], Xuelei Fu[2], Yiming Wang[2], Song Gong[1,3], Tuan Guo[6] and Zhengying Li[2,4*]

[1]Division of Trauma Surgery, Emergency Surgery & Surgical Critical, Tongji Trauma Center, Tongji Hospital, Tongji Medical College, Huazhong University of Science and Technology, Wuhan 430030, China; [2]School of Information Engineering, Wuhan University of Technology, Wuhan 430070, China; [3]Department of Emergency and Critical Care Medicine, Tongji Hospital, Tongji Medical College, Huazhong University of Science and Technology, Wuhan 430030, China; [4]National Engineering Research Center of Fiber Optic Sensing Technology and Networks, State Key Laboratory of Advanced Technology for Materials Synthesis and Processing, Wuhan University of Technology, Wuhan 430070, China; [5]Hubei Key Laboratory of Micro-Nanoelectronic Materials and Devices, Hubei Collaborative Innovation Center for Advanced Organic Chemical Materials, Ministry of Education Key Laboratory of Green Preparation and Application for Functional Materials, and School of Microelectronics, Hubei University, Wuhan 430062, China; [6]Institute of Photonics Technology, Jinan University, Guangzhou 510632, China.

[†]These authors contributed equally to this work.

*Correspondence: ZY Li, E-mail: zhyli@whut.edu.cn; XH Liu, E-mail: hualiu@tjh.tjmu.edu.cn

This file includes:

Supplementary information for this paper is available at https://doi.org/10.29026/oes.2025.240034

Section 1: The first principles computation of $Ti_3C_2T_x$

First-principles calculations with the Cambridge Serial Total Energy Package (CASTEP) were performed to analyze the phonon spectra and phonon density of state (PDOS). The optimized lattice parameters and IFCs are obtained from the total energy calculations by using plane augmented wave method based on density functional theory with Vienna ab initio simulation package (VASP)[S1–S5]. The electronic wave functions are expanded in a plane wave basis set with an energy cutoff of 500 eV. Such a high cutoff was found necessary to converge to the phonon dispersion curves. The Brillouin zone was sampled with 2 × 2 × 1 *k*-points Monkhorst-Pack meshes for primitive cells of hexagonal structure (P63/mmc space group) of $Ti_3C_2T_x$.

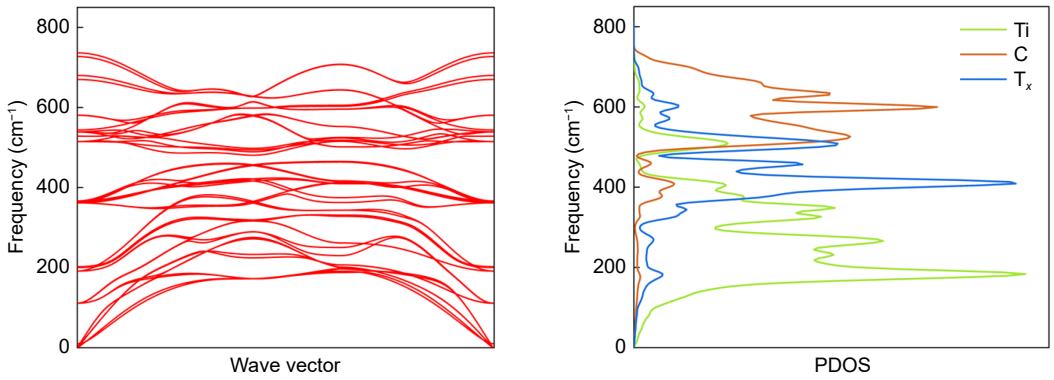

Fig. S1 | Calculated phonon dispersion relation along the high symmetry directions and projected phonon DOS of $Ti_3C_2T_x$.

Section 2: Characterization of photothermal conversion of $Ti_3C_2T_x$

In addition to the light absorption of a light-to-heat material, the photothermal conversion efficiency is another essential factor that directly quantifies the absorbed energy transferred to thermal energy, instead of radiative re-emission of photons[S6,S7]. One straightforward method for determining the conversion efficiency is to measure the temperature increase and calculate the heat generation induced by incident light[S7–S9]. The detailed calculation was carried out using the following equations: The total energy balance of this system is given by the following equation[S10,S11]:

$$\sum_i m_i C_{\mathrm{p},i} \frac{\mathrm{d}T}{\mathrm{d}t} = Q_{\mathrm{NPs}} + Q_{\mathrm{s}} - Q_{\mathrm{loss}} \,, \tag{S1}$$

where m and C_{p} are the mass and heat capacity, respectively. The suffix i of m and C_{p} refers to solvent (water) or dispersed matter (nanoparticles). T is the solution temperature. Q_{NPs} is the photothermal energy absorbed by MXenes per second:

$$Q_{\mathrm{NPs}} = I(1 - 10^{-A_\lambda})\eta \,, \tag{S2}$$

where I is the laser power, A_λ is the absorbance of MXenes at the wavelength of 1064 nm in aqueous solution, and η is the photothermal conversion efficiency of MXenes which means the ratio of absorbed light energy converting to thermal energy. Q_{loss} is thermal energy lost to the surroundings:

$$Q_{\mathrm{loss}} = hA\Delta T \,, \tag{S3}$$

where h is the heat transfer coefficient, A is the surface area of the container, and ΔT is the changed temperature, which is referred to T–T_{sur} (T and T_{sur} are the solution temperature and ambient temperature of the surrounding, respectively). Q_{s} is the heat associated with the light absorbed by solvent per second. In the situation of heating pure water, the heat input is equal to the heat output at the maximum steady-statue temperature, so the equation can be:

$$Q_{\mathrm{s}} = Q_{\mathrm{loss}} = hA\Delta T_{\mathrm{max,water}} \,, \tag{S4}$$

where $\Delta T_{\mathrm{max,water}}$ is the temperature change of water at the maximum steady-state temperature. As it to the experiment of MXenes dispersion, the heat inputs are the heat generated by nanoparticles (Q_{NPs}) and the heat generated by water

(Q_s), which is equal to the heat out put at the maximum steady-statue temperature, so the equation can be:

$$Q_{NPs} + Q_S = Q_{loss} = hA\Delta T_{max,mix} \ , \tag{S5}$$

where $\Delta T_{max,mix}$ is the temperature change of the MXenes dispersion at the maximum steady state temperature. According to the Eqs. (S2), (S4) and (S5), the photothermal conversion efficiency η can be written as:

$$\eta = \frac{Q}{E} = \frac{cm\Delta T}{IAt} = \frac{hA(\Delta T_{max,mix} - \Delta T_{max,water})}{I(1-10^{-A_\lambda})} \ , \tag{S6}$$

where Q is the generated thermal energy by the absorber, E represents the total energy of the incoming light, c and m denote the specific heat and mass of the photothermal material, ΔT is the temperature increase of the material under the light irradiation. In this equation, only is hA unknown. In order to get the hA, we introduce φ, which is defined as the ratio of ΔT to ΔT_{max}:

$$\varphi = \frac{\Delta T}{\Delta T_{max}} \ . \tag{S7}$$

Substituting Eq. (S7) into Eq. (S1):

$$\frac{d\varphi}{dt} = \frac{hA\left(\frac{Q_{NPs} + Q_S}{hA\Delta T_{max}} - \varphi\right)}{\sum_i m_i C_{p,i}} \ . \tag{S8}$$

When the pulse laser was shut off, the , Eq. (S8) could be expressed to:

$$dt = -\frac{\sum_i m_i C_{p,i}}{hA} \cdot \frac{d\varphi}{\varphi} \ . \tag{S9}$$

Compared with solvent, mass of MXenes was too little. Generally, the specific heat of water is much higher than other materials. Consequently, the m and C_p of MXenes were neglected. Equation (S9) changes the expression:

$$t = -\frac{\sum_i m_i C_{p,i}}{hA} \ln\varphi = -\frac{m_{water}C_{water}}{hA} \ln\varphi = k(-\ln\varphi) \ . \tag{S10}$$

According to the method for calculating photothermal conversion efficiency[S12], the slope of the fitted curve is obtained by linearly fitting the time and $-\ln(\varphi)$ data, from which the photothermal conversion efficiency is then calculated. The equation of the photothermal conversion efficiency η can then be expressed as

$$\eta = \frac{m_{water}C_{water}(\Delta T_{max,mix} - \Delta T_{max,water})}{kI(1-10^{-A_\lambda})} \approx 92\% \ . \tag{S11}$$

Table S1 | The parameters and the photothermal efficiencies of MXenes.

m_{water} (g)	C_{water} (J·°C^{-1}·g^{-1})	$\Delta T_{max,mix}$ (°C)	$\Delta T_{max,water}$ (°C)	I (W)	A_λ	k	η
0.45	4.2	22.1	1.6	0.27	1.11	168.58	92%

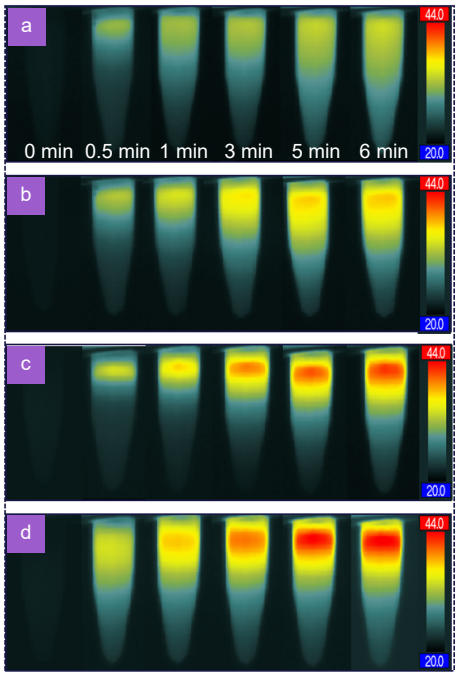

Fig. S2 | The infrared thermal images of $Ti_3C_2T_x$ concentration: (**a**) 1.0 wt%, (**b**) 0.8 wt%, (**c**) 0.5 wt%, (**d**) 0.25 wt% at different times (1064 nm, 0.45 g, 0.27 W).

Section 3: Photoacoustic conversion

The definition expression of photoacoustic pressure

The photoacoustic signal amplitude (P) can be rewritten as[S13]

$$P = \Gamma \cdot A \cdot \frac{F}{l}, \tag{S12}$$

here, $\Gamma = \beta c^2/C_p$ represents the dimensionless Grüneisen parameter, where A is the light absorption ($0 < A < 1$; dimensionless), F is the laser fluence ($J{\cdot}m^{-2}$), l is the characteristic length (m), β is the volumetric thermal-expansion coefficient ($°C^{-1}$), C_p is the specific heat capacity at constant pressure ($J{\cdot}kg^{-1}{\cdot}K^{-1}$), and c is the sound speed ($m{\cdot}s^{-1}$). According to equation (12), the amplitude of the photoacoustic signal is positively correlated with the thermal expansion coefficient. The temperature dependence of the thermal expansion coefficient of PDMS shows that the β value remains around 3.2×10^{-4} $°C^{-1}$ up to 300 °C, which is consistent with values reported in the literature[S14]. However, beyond 300 °C, the thermal expansion coefficient rapidly decreases due to the high-temperature degradation of PDMS.

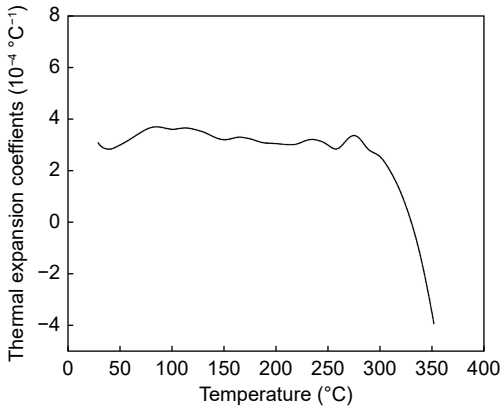

Fig. S3 | The temperature dependence of the thermal expansion coefficient of PDMS.

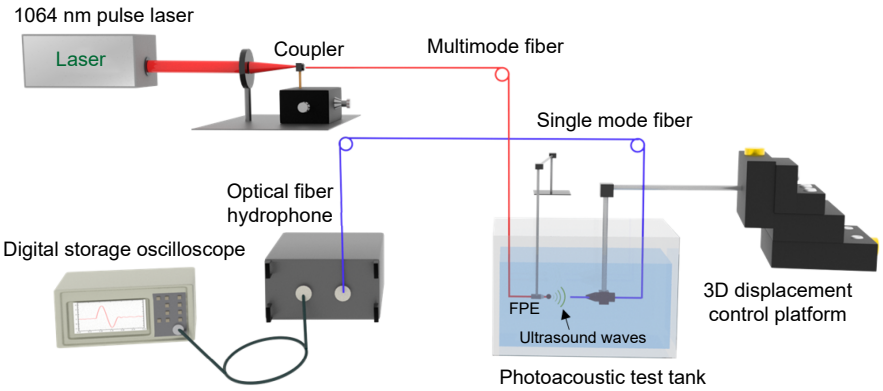

Fig. S4 | Test system of fiber-optic photoacoustic emitter (FPE).

Table S2 | Performance summary of representative photoacoustic emitters.

Photoacoustic emitter	Optical absorption materials		Emitter characteristic			ref.
	photothermal (%)	light absorption (μm^{-1})	CF (MHz)	−6dB BW (%)	η ($\times10^{-2}$)	
Functionalized MWCNTs -PDMS	~50	1	28.5	~140	–	ref. [S15,S16]
CNTs array-PDMS	–	30.3	20.2	152	0.251	ref. [S17]
$MAPbI_3$–PDMS	–	10	29.2	140	2.97	ref. [S18]
MWCNTs-PMMA	~50	1	~30	147	–	ref. [S16,S19]
CSPs-PDMS	~54	~1	13.5	149	0.441	ref. [S20,S21]
IR 144-UV adhesive	–	–	~4	~75%	–	ref. [S22]
$Ti_3C_2T_x$–PDMS	**92**	**~0.5**[S23]	**4**	**162**	**–**	**This work**

Note: MWCNTs: multiwalled carbon nanotube, $MAPbI_3$: Methylamine lead iodine, PMMA: polymethyl methacrylate, CSPs: andle-soot carbon nanoparticles.

Analytical solution of photoacoustic pressure

The photoacoustic emitter, based on the photoacoustic effect, converts light energy into mechanical energy[S13–S24]. Thermoacoustic coupling theory serves as an important theoretical foundation for photoacoustic emitters. In the $Ti_3C_2T_x$/PDMS fiber-optic photoacoustic emitter, $Ti_3C_2T_x$ represents a light-absorbing material that converts light energy into heat energy and transfers this heat energy to the surrounding PDMS. The diffusion of heat in non-viscous media can be described by the following equation[S18,S25–S28]:

$$\kappa_i \nabla^2 T_i - \frac{\kappa_i}{\alpha_i}\frac{\partial T_i}{\partial t} = -S_i \,, \tag{S13}$$

where κ, α, t, T, and S are the thermal conductivity, the thermal diffusivity, the time, the temperature, and an arbitrary thermal source, respectively. The fiber-optic, $Ti_3C_2T_x$/PDMS, and water are labeled as 1, 2 and 3, consecutively.

Because the pulse width of the laser is ns level, the thermal diffusion during the acoustic generation can be neglected, yielding the equation.

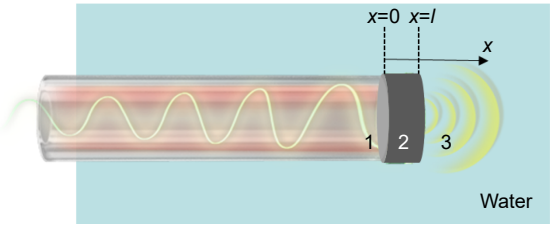

Fig. S5 | Structure diagram of fiber-optic photoacoustic emitter.

$$\frac{\partial^2 T_i}{\partial t^2} = \frac{1}{\rho_i C_{P_i}} \frac{\partial S_i}{\partial t} , \tag{S14}$$

where ρ is the density and C_P is the thermal capacity which equals $C_{P_i} = \kappa_i/\rho_i\alpha_i$.

Therefore, the thermomechanical coupling equation in the medium can be expressed by the following equation.

$$\nabla^2 P_i - \frac{1}{c_i^2}\frac{\partial^2 P_i}{\partial t^2} = -\rho_i \beta_{T_i} \frac{\partial^2 T_i}{\partial t^2} , \tag{S15}$$

where P is the pressure, β_T is the thermal volume expansion constant, and c is the acoustic speed in the medium.

Substituting the Eq. (S14) into Eq. (S15), We can obtain the equation of thermally induced mechanical vibration (pressure).

$$\nabla^2 P_i - \frac{1}{c_i^2}\frac{\partial^2 P_i}{\partial t^2} = -\frac{\beta_{T_i}}{C_{P_i}} \frac{\partial S_i}{\partial t} . \tag{S16}$$

The spatial and temporal distribution of heat generated in the form of radiation-free transition after the heat source (2nd medium) absorbs light can be expressed as the following equation.

$$S_2 = \gamma I_0 \mathrm{e}^{-\gamma x} \mathrm{e}^{\mathrm{j}\omega t} , \tag{S17}$$

where γ is the light absorption coefficient, I_0 is the intensity of the incident light, ω is the angular frequency, t is the time, and x is the coordinate. The time-dependent harmonic pressure response can be expressed as $P_i = \overline{P_i}\mathrm{e}^{\mathrm{j}\omega t}$, and the acoustic wave equation becomes.

$$\frac{\mathrm{d}^2 \overline{P_i}}{\mathrm{d}x^2} - k_i^2 \overline{P_i} = -\frac{\mathrm{j}\omega\beta_{T_i}}{C_{P_i}} \overline{S_i} , \tag{S18}$$

where $k_i = \mathrm{j}\omega/c_i$, $\overline{S_2} = \gamma I_0 \mathrm{e}^{-\gamma x}$ and $\overline{S_1} = \overline{S_3} = 0$.

The acoustic pressure amplitude in each medium can thus be solved as

$$\left.\begin{aligned} \overline{P_1} &= D_1 \mathrm{e}^{-k_1(x)} \\ \overline{P_2} &= D_{21}\mathrm{e}^{k_2 x} + D_{22} e^{-k_2 x} - \frac{\mathrm{j}\omega\beta_{T_2}}{C_{P_i}} \left(\frac{\gamma I_0}{\gamma^2 - k_2^2}\mathrm{e}^{-\gamma x}\right) \\ \overline{P_3} &= D_3 \mathrm{e}^{k_3(x-l)} \end{aligned}\right\} . \tag{S19}$$

where D_1, D_{21}, D_{22} and D_3 are constants related to the optical and thermal properties of materials and can be determined by the boundary conditions. Due to the continuity of the acoustic medium at the interfaces 1 and 2, and 2 and 3, the acoustic pressure and sound velocity of the boundary medium can be expressed by the following equation.

$$\left.\begin{aligned} \overline{P_1}\big|_{x=0} &= \overline{P_2}\big|_{x=0} \\ \overline{P_2}\big|_{x=l} &= \overline{P_3}\big|_{x=l} \end{aligned}\right\} , \tag{S20}$$

$$\left.\begin{aligned} v_1\big|_{x=0} &= v_2\big|_{x=0} \\ v_2\big|_{x=l} &= v_3\big|_{x=l} \end{aligned}\right\} , \tag{S21}$$

with the pressure and the velocity related by $v_i = -(1/\mathrm{j}\omega\rho_i)\mathrm{d}\overline{P_i}/\mathrm{d}x$. A set of equations for the undetermined constants is attained as

$$\begin{pmatrix} -1 & \mathrm{e}^{k_2 l} & \mathrm{e}^{-k_2 l} & 0 \\ 0 & 1 & 1 & -1 \\ \dfrac{k_1}{\rho_1} & \dfrac{k_2}{\rho_2}\mathrm{e}^{k_2 l} & -\dfrac{k_2}{\rho_2}\mathrm{e}^{-k_2 l} & 0 \\ 0 & \dfrac{k_2}{\rho_2} & -\dfrac{k_2}{\rho_2} & -\dfrac{k_3}{\rho_3} \end{pmatrix} \begin{pmatrix} D_1 \\ D_{21} \\ D_{22} \\ D_3 \end{pmatrix} = \begin{pmatrix} R_1 \\ R_2 \\ R_3 \\ R_4 \end{pmatrix} , \tag{S22}$$

where

$$\left.\begin{aligned} R_1 &= \frac{\mathrm{j}\omega\beta_{T_2}}{C_{P_2}}\left(\frac{\gamma I_0}{\gamma^2-k_2^2}\mathrm{e}^{-\gamma l}\right) \\ R_2 &= \frac{\mathrm{j}\omega\beta_{T_2}}{C_{P_2}}\left(\frac{\gamma I_0}{\gamma^2-k_2^2}\right) \\ R_3 &= -\frac{1}{\rho_2}\frac{\mathrm{j}\omega\beta_{T_2}}{C_{P_2}}\left(\frac{\gamma^2 I_0}{\gamma^2-k_2^2}\mathrm{e}^{-\gamma l}\right) \\ R_4 &= -\frac{1}{\rho_2}\frac{\mathrm{j}\omega\beta_{T_2}}{C_{P_2}}\kappa_2\left(\frac{\gamma^2 I_0}{\gamma^2-k_2^2}\right) \end{aligned}\right\}. \tag{S23}$$

It can be expressed by the following equation.

$$D_3 = \frac{Z_2\beta_{T_2}\gamma I_0}{\gamma^2-k_2^2}\frac{\alpha_2}{\kappa_2}\frac{2(\gamma+k_2R_{23})-(\gamma+k_2)(1+R_{23})\mathrm{e}^{(k_2-\gamma)l}-(\gamma-k_2)(1-R_{23})\mathrm{e}^{-(k_2+\gamma)l}}{(1+R_{21})(1+R_{23})\mathrm{e}^{k_2 l}-(1-R_{21})(1-R_{23})\mathrm{e}^{-k_2 l}}. \tag{S24}$$

Based on the equation above, the acoustic pressure amplitude at the water can be expressed as:

$$P(x,t) = D_3\mathrm{e}^{\mathrm{j}\omega t-k_1(x-l)}. \tag{S25}$$

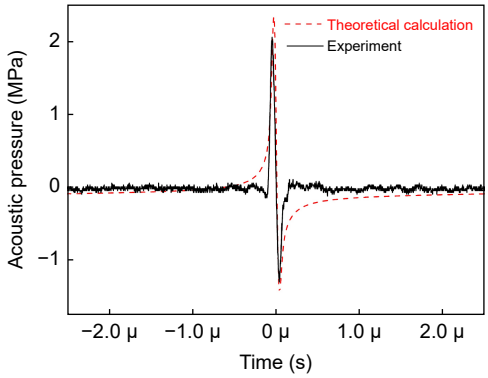

Fig. S6 | Theoretical (red dotted line) and experimental (black solid line) results of acoustic pressure of FPE.

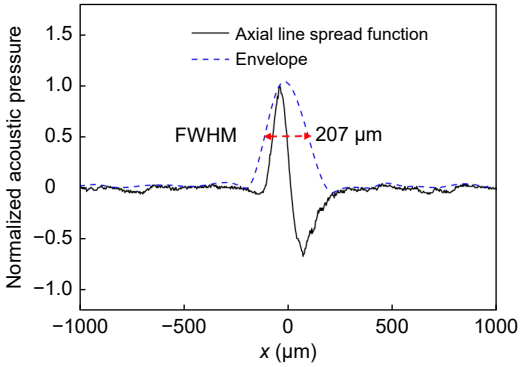

Fig. S7 | Axial line spread function (black solid curve) and its envelope (blue dashed curve).

Section 4: Animal experiment

The rationale of the $Ti_3C_2T_x$-PDMS composite fiber-optic photoacoustic emitter for minimally invasive neural stimulation

The pulse laser is applied to the photoacoustic emitter, where the light absorption material $Ti_3C_2T_x$ absorbs the light and converts it into heat, resulting in a temperature increase. This heat is then transferred to the surrounding thermal expansion material, PDMS, causing it to heat up and undergo thermal expansion. The periodic nature of the pulsed laser induces thermal expansion and contraction in the PDMS, generating ultrasound waves. These ultrasound waves

induce changes in neural potential, enabling the modulation of neural activity in mice. In our animal experiments, the most important question, and the one we needed to confirm from the beginning, was whether our ultrasound waves could activate neurons. Therefore, we conducted two experiments.

Firstly, we examined the expression of c-fos following stimulation (Fig. 4(a–d)). Using the TTA-cfos-TRE-tight system, we found that photoacoustic stimulation could specifically activate neurons. In this system, the TTA transcription factor binds to the TRE sequence to drive c-fos expression, which is a well-recognized marker of neuronal activation. The tight version of the system ensures high specificity, allowing us to detect neuronal activation with minimal background expression.

Second, we employed in vivo fiber photometry (Fig. 4(e, f)), where we observed an increase in intracellular calcium flux in neurons. This increase indicates that the photoacoustic stimulation effectively depolarized neurons, leading to calcium entry through voltage-gated calcium channels or other pathways. These findings further confirm that our material can specifically and functionally activate neurons.

Virus preparations

We used the following virus vectors carrying the following specific genes purchased from BrainVTA (Wuhan): rAAV-CaMKIIa-GCaMP6s-WPRE-hGH-polyA, rAAV-cfos-TTA, rAAV-TRE-tight-mCherry. The viral titers were in the range of 3–8 × 10^{12} genome copies/ml.

Stereotactic surgeries and doxycycline (DOX) administration

Stereotactic surgeries were performed on the mice under anesthesia induced by inhaled isoflurane (1.5%). Once the tail-clamp reflex was lost, the head was securely fixed in a stereotaxic frame. The skull was then exposed and cleaned using 3% H_2O_2. A mixture of 500 nL rAAV-cfos-TTA and rAAV-TRE-tight-mCherry (1:1) was injected into the right mPFC at coordinates of bregma +2.1 mm, AP +0.5 mm, DV 2.5 mm relative to the bregma, using a 10 μL Hamilton syringe at a rate of 0.1 μL/min. Ten minutes post-injection, the needle was slowly withdrawn. Subsequently, a FPE was implanted into the same site above the injection site, ensuring the tip of the FPE was located at DV 2.2 mm. Following virus injection, mice were maintained with DOX (1 mg/mL) in their drinking water for 4 weeks, with DOX administration ceased two days before photoacoustic stimulation. On the day of photoacoustic stimulation, mice were administered DOX intraperitoneally at a dose of 1 g/kg, followed by daily administration of DOX (1 mg/mL) in water. This regimen allowed for mCherry expression over a 4 week period. Subsequently, the mice were euthanized, and brain were sliced to detect photoacoustic activated neurons (mCherry positive neurons).

For fiber-photometry experiments, mice were injected with rAAV-CaMKIIa-GCaMP6s-WPRE-hGH-polyA (200 nL) into the right mPFC using a 10 μL Hamil-ton syringe at a rate of 0.1 μL/min. Ten minutes after injection, the needle was s-lowly removed. Subsequently, an optic fiber ferrule (200 μm in diameter, 0.37 N-A, Inper Technology Co., Ltd) was implanted at a 20 degree angle from posterior to anterior, targeting coordinates of bregma +1.19 mm, AP +0.5 mm, DV 2.6 mm. Additionally, a FPE was implanted following the same procedure as previousl-*y* described. Experiments conducted 2 weeks post-implantation to allow for virus expression and surgical recovery.

c-fos imaging

Mice were perfused intracardially with 4% paraformaldehyde in phosphate-buffered saline (PBS). Following perfusion, brains were post fixed overnight at 4 °C and subsequently dehydrated in 20% and 30% sucrose solutions. Coronal brain sections of 30 μm thickness were sliced using a Leica 1860 vibratome. The brain slices were permeabilized with 0.3% Triton *X*-100 in PBS for 10 minutes and then blocked with 5% bovine serum albumin (BSA) in PBS for 30 minutes. Nuclei were stained with DAPI, and the sections were covers lipped using fluorescent mounting medium. Imaging was performed using an Olympus VS120 microscope.

Photoacoustic stimulation protocol

For detecting c-fos expression induced by photoacoustic stimulation, the intensity of the photoacoustic stimulation administered was 0.8 MPa for 1 hour. For fiber photometry recording, mice were subjected to baseline recordings for 2

minutes, followed by 2 minute sessions of photoacoustic stimulation at intensities of 0.4, 0.6, and 0.8 MPa. Simultaneously, the brightness of the GCaMP probe at a wavelength of 470 nm was recorded. In the behavioral tests, photoacoustic stimulation administered after SDS was at an intensity of 0.8 MPa for 1 hour.

In vivo fiber photometry

The fiber photometry system (Inper Technology Co., Ltd) utilized a 473 nm excitation light emitted from LEDs, reflected off a dichroic mirror with a 435–488 nm reflection band and a 502–730 nm transmission band, and then coupled into a 200 μm 0.37 NA fiber-optic by an objective lens. To assess changes in neuronal activity in response to photoacoustic stimulation, we initially recorded a 2 minute baseline. Subsequently, we administered a gradient of increasing photoacoustic intensities, including 0.4, 0.6, and 0.8 MPa, with each interval lasting 2 minutes. Concurrently, we synchronously recorded the neuronal calcium activity of the mPFC as alterations in GCaMP6s fluorescence using in vivo calcium imaging. The raw calcium fluorescence data were then normalized and converted to z-scored traces. The fluorescence change values were derived by calculating $\Delta F/F_0$, where ΔF represents the variation in fluorescence between each sampling (sampling frequency 20 Hz), and F_0 denotes the averaged fluorescence baseline recorded during the 2 minute baseline period.

Statistical analysis

The data were analyzed using GraphPad Prism 9.0 (GraphPad Software Inc., CA, USA). Normality was assessed using the *Shapiro-Wilk* test. Paired t-tests were used for the analysis of behavioral tests, with p values less than 0.05 considered statistically significant.

Behavioral tests

The open-field test (OFT) was conducted to assess anxiety-like behavior. Briefly, mice were gently placed into the open field and allowed to explore the area for 10 minutes. For the three chamber social interaction test (3 chamber test) to evaluate social preference in mice, the apparatus consisted of three chambers: left, center, and right. During the habituation phase, the test mouse freely explored all three chambers for 10 minutes to acclimate to the environment. In session 1, a novel mouse was placed inside a small cage in the left chamber, while the right chamber remained empty. The tested mouse was then allowed to explore all three chambers for 10 minutes. After a 5 minute interval, in session 2, another novel mouse was introduced into the cage in the right chamber. The tested mouse was again to explore the apparatus for 10 minutes.

All behavioral experiments were recorded using a camera and analyzed using DeepLabCut[S29]. In summary, we selected 6 videos and extracted 120 frames from each video to label 4 body parts of the mice (nose, left ear, right ear and tail base). The network was trained using 180,000 iterations, resulting in a training error of 2.21 pixels and a test error of 2.67 pixels with a cutoff of 0.6. Once the network was trained, we applied it to analyze all videos. Subsequently, a custom Python code was used to calculate the traveled distance and the duration spent in the center zone in the OFT. In the 3 chamber test, the time spent in each chamber was recorded, and the percentage of time spent in the right chamber relative to the total time was calculated.

Behavioral design

After 3 days post-implantation of fiber-optic photoacoustic emitter, mice underwent OFT and 3 chamber test (before fight). Subsequently, mice were co-housed with a CD1 mouse for 1 hour (fighting, SDS). Following SDS exposure, OFT and 3 chamber test were conducted (after fight). Then, mice received photoacoustic stimulation (0.8 MPa for 1 hour, n=4). After 10 days, the same experiments were repeated, except that mouse received sham stimulation, where the patch cable was connected but no stimulation was delivered (n=4).

Section 5: Legends for movies S1 to S2

Movie S1

Three chamber test, after stimulation session 1

The apparatus consisted of left, center, and right chambers. In session 1, a novel mouse was placed inside a small cage in the left chamber, while the right chamber remained empty. The tested mouse explored all three chambers for 10 minutes. This video depicts the behavior of the tested mouse after stimulation in session 1, correlated to Fig. 5(g).

Movie S2

Three-chamber test, after stimulation session 2

After a 5 minute interval, in session 2, another novel mouse was introduced into the right chamber. The tested mouse explored the apparatus for 10 minutes. This video depicts the behavior of the tested mouse after stimulation in session 2, correlated to Fig. 5(g).

References

S1. Faraji M, Bafekry A, Fadlallah MM et al. Surface modification of titanium carbide MXene monolayers (Ti_2C and Ti_3C_2) *via* chalcogenide and halogenide atoms. *Phys. Chem Chem Phys* **23**, 15319–15328 (2021).

S2. Perdew JP, Burke K, Ernzerhof M. Generalized gradient approximation made simple. *Phys Rev Lett* **77**, 3865–3868 (1996).

S3. Wang YF, Xu YH, Hu ML et al. MXenes: focus on optical and electronic properties and corresponding applications. *Nanophotonics* **9**, 1601–1620 (2020).

S4. Kresse G, Hafner J. *Ab initio* molecular dynamics for liquid metals. *Phys Rev B* **47**, 558–561 (1993).

S5. Kresse G, Furthmüller J. Efficient iterative schemes for *ab initio* total-energy calculations using a plane-wave basis set. *Phys Rev B* **54**, 11169–11186 (1996).

S6. Lu HZ, Wang JH, LI HM et al. Efficient photothermal conversion of MXenes and their application in biomedicine. *Mater Chem Front* **7**, 4372–4399 (2023).

S7. Cui XM, Ruan QF, Zhuo XL et al. Photothermal nanomaterials: a powerful light-to-heat converter. *Chem Rev* **123**, 6891–6952 (2023).

S8. Zeng J, Goldfeld D, Xia YN. A plasmon-assisted optofluidic (PAOF) system for measuring the photothermal conversion efficiencies of gold nanostructures and controlling an electrical switch. *Angew Chem Int Ed* **52**, 4169–4173 (2013).

S9. Xiao LH, Chen X, Yang XY et al. Recent advances in polymer-based photothermal materials for biological applications. *ACS Appl Polym Mater* **2**, 4273–4288 (2020).

S10. Ren WZ, Yan Y, Zeng LY et al. A near infrared light triggered hydrogenated black TiO_2 for cancer photothermal therapy. *Adv. Healthcare Mater* **4**, 1526–1536 (2015).

S11. Zhang M, Xu ZH, Chen JQ et al. Recent advances on nanomaterials-based photothermal sensing systems. *TrAC-Trend Anal Chem* **177**, 117801 (2024).

S12. Feng YC, Lu SY, Zhao Q et al. Controlled phase transition of the onion-like carbon nanostructure for photothermal cancer therapy. *ACS Appl Nano Mater* **7**, 7008–7017 (2024).

S13. Lee T, Baac HW, Li QC et al. Efficient photoacoustic conversion in optical nanomaterials and composites. *Adv Optical Mater* **6**, 1800491 (2018).

S14. Zhang GG, Sun YL, Qian BK et al. Experimental study on mechanical performance of polydimethylsiloxane (PDMS) at various temperatures. *Polymer Testing* **90**, 106670 (2020).

S15. Noimark S, Colchester RJ, Blackburn BJ et al. Carbon-nanotube-PDMS composite coatings on optical fibers for all-optical ultrasound imaging. *Adv Funct Mater* **26**, 8390–8396 (2016).

S16. Maestro LM, Haro-González P, del Rosal B et al. Heating efficiency of multi-walled carbon nanotubes in the first and second biological windows. *Nanoscale* **5**, 7882–7889 (2013).

S17. Li JP, Xu JB, Liu XL et al. A novel CNTs array-PDMS composite with anisotropic thermal conductivity for optoacoustic transducer applications. *Compos Part B Eng* **196**, 108073 (2020).

S18. Du XY, Li JP, Niu GD et al. Lead halide perovskite for efficient optoacoustic conversion and application toward high-resolution ultrasound imaging. *Nat Commun* **12**, 3348 (2021).

S19. Wang L, Zhao YW, Zheng B et al. Ultrawide-bandwidth high-resolution all-optical intravascular ultrasound using miniaturized photoacoustic transducer. *Sci Adv* **9**, eadg8600 (2023).

S20. Chang WY, Huang WB, Kim J et al. Candle soot nanoparticles-polydimethylsiloxane composites for laser ultrasound transducers. *Appl Phys Lett* **107**, 161903 (2015).

S21. Wei CX, Jin X, Wu CW et al. Carbon spheres with high photothermal conversion efficiency for photothermal therapy of tumor. *Diam Relat Mater* **126**, 109048 (2022).

S22. Yang G, Huang HB, Luo HB et al. Fiber endface photoacoustic generator for quantitative photoacoustic tomography. *Opt Lett* **46**, 2706–2709 (2021).

S23. Tan KH, Samylingam L, Aslfattahi N et al. Optical and conductivity studies of polyvinyl alcohol-MXene (PVA-MXene) nanocomposite thin

films for electronic applications. *Opt Laser Technol* **136**, 106772 (2021).

S24. Chen SL. Review of Laser-generated ultrasound transmitters and their applications to all-optical ultrasound transducers and imaging. *Appl Sci* **7**, 25 (2017).

S25. Noimark S, Colchester RJ, Poduval RK et al. Polydimethylsiloxane composites for optical ultrasound generation and multimodality imaging. *Adv Funct Mater* **28**, 1704919 (2018).

S26. Huang WB, Chang WY, Kim J et al. A novel laser ultrasound transducer using candle soot carbon nanoparticles. *IEEE Trans Nanotechnol* **15**, 395–401 (2016).

S27. Lee T, Li QC, Guo LJ. Out-coupling of longitudinal photoacoustic pulses by mitigating the phase cancellation. *Sci Rep* **6**, 21511 (2016).

S28. Chen ZY, Wu Y, Yang Y et al. Multilayered carbon nanotube yarn based optoacoustic transducer with high energy conversion efficiency for ultrasound application. *Nano Energy* **46**, 314–321 (2018).

S29. Mathis A, Mamidanna P, Cury KM et al. Deep LabCut: markerless pose estimation of user-defined body parts with deep learning. *Nat Neurosci* **21**, 1281–1289 (2018).